FLOW AND HEAT TRANSFER CHARACTERISTICS OF HIGH-PRESSURE NATURAL GAS IN THE GAPS OF HIGH-SPEED MOTORS WITH A HIGH RADIUS RATIO

Qiang ZHAO [1, 2], Yichao YUAN [1*]

[*1]School of Energy and Power Engineering, University of Shanghai for Science and Technology, Jungong Road 516, 200093 Shanghai, China

[2]Wolong Electric Nanyang Explosion Protection Group Co., LTD, Dushan Road 1801, 473000, Nanyang, China

[*] Corresponding author; E-mail: yuanyichao@usst.edu.cn

A motor stator-gap-rotor model is established based on the numerical heat transfer theory by using the finite volume method. The flow evolution of high-pressure natural gas in the gap with a radius ratio of 0.971 is investigated. The results demonstrate that the flow patterns of high-pressure natural gas in the motor gap can be categorized into turbulent, spiral Taylor-Couette, and turbulent Taylor-Couette flow; the flow ranges are determined based on the Ta/Re^2. Then, the flow and heat transfer characteristics of the cooling medium in the gap under different flow regimes as well as the mechanism of locally enhanced heat transfer in the gap by the Taylor-Couette flow are explored. Finally, the mathematical expressions for the Nusselt number of motor gap are determined in terms of the Reynolds number, Taylor number, and Prandtl number by fitting using the Levenberg-Marquardt and global optimization methods. Using these expressions, the flow and heat transfer characteristics in the motor gap can be predicted. Overall, this study provides useful and novel insights on the design of cooling systems for high-speed motors.

Keywords: *high radius ratio; high-pressure natural gas; Taylor-Couette flow; high-speed motor; numerical simulation*

1. Introduction

High-speed induction motors are directly connected to centrifugal compressors for transporting natural gas. These motors are directly cooled by high-pressure natural gas, so fan-powered components and cooling heat sinks are not needed, resulting in a high degree of integration and excellent reliability of the system. Hence, high-speed induction motors are widely used in onshore and offshore natural gas pipelines and underground gas storage reservoirs [1-2]. Under the action of high-speed rotation, the high-frequency current and high-frequency magnetic density of the induction motor cause serious heating of its stator and rotor [3-4]. Meanwhile, to ensure sufficient strength of the motor rotor in high-speed operation, the solid rotor structure is usually used. There is no radial ventilation channel between the stator and the rotor, and the narrow annular air gap between the rotor and the stator is the main ventilation and heat transfer area of the motor. Different from traditional air-cooled motors, the density of high-pressure natural gas is significantly higher than that of air, and the rotational speed of high-speed induction motors is several times that of ordinary motors. Further, the

Taylor number of natural gas in the air gap is much larger than the critical value of turbulent Taylor vortex (10^4), so the natural gas can easily form a Taylor vortex in the air gap [5], which makes the flow state in the air gap of the motors more complicated. Therefore, it is necessary to study the flow and heat transfer characteristics of natural gas cooling medium in the air gap.

The study of the flow and heat transfer characteristics in the air gap of the motor can help to improve the efficiency of the motor and reduce the operating cost of the motor. Saari [5] summarized the classification rules for the four flow regimes: laminar flow, laminar flow with Taylor-Couette flow, turbulent Taylor-Couette flow, and turbulent flow with axial Reynolds number and Taylor number in the range of 0-2000 and 0-10^6, respectively. Naseem et al. [6] investigated the flow of silicone oil AK20 in an annular air gap with a radius ratio of 0.1 by using particle image velocimetry (PIV) experiments. The results revealed that in a specific range of Reynolds number, increasing or decreasing the rotational Reynolds number did not have a significant effect on the shape of the flow structure, but when the rotational Reynolds number continued to increase, the flow structure showed random behavior. Tanaka et al. [7] investigated the flow evolution from laminar to turbulent regime in an annular air gap with radius ratios ranging from 0.2 to 0.5 and rotational Reynolds numbers ranging from 500 to 4000 by using three-dimensional direct numerical simulations and determined the transition thresholds for radius ratios of 0.2 and 0.3. Sznitko [8] used numerical simulations to examine the flow characteristics in an annular air gap with radius ratios of 0.25-0.6 and rotational Reynolds numbers of 100-4200 and obtained the critical values for the transition of flow regimes in annular air gaps with different radius ratios. Kusumastuti et al. [9] experimentally studied the effect of volume ratio of water to waste edible oil on the distribution of shear stress and energy loss in a Taylor-Couette column, where the mixed fluid of waste oil and water was placed in an annular air gap with a radius ratio of 0.6. Fujii et al. [10] used numerical simulations to investigate the distribution of flow field and temperature field in an annular air gap with a radius ratio of 0.767 and Taylor number of 505.6-2559.66, and they proposed an empirical correlation of Nusselt number. Swann et al. [11] designed a high Taylor number flow experimental platform using air and supercritical carbon dioxide as the experimental medium. Further, the heat transfer data were obtained under a radius ratio of 0.76 and Taylor numbers of $8.8 \pm 0.8 \times 10^7$ and $1.32 \pm 0.8 \times 10^{12}$. Qin et al. [12] numerically simulated the flow and heat transfer characteristics of high-pressure CO_2 in an annular air gap with radius ratios of 0.83, 0.87, 0.91, and 0.95 and Taylor numbers of 1.83×10^9-1.66×10^{11}. The results show that the heat transfer performance decreases with the increase of the gap, and a wide gap facilitated flow stabilization by delaying the development of Taylor vortices and reducing their effect on heat transfer. In addition, the flow and heat transfer characteristics of traditional cooling medium such as air [13], water [14], and oil [15] in the air gap of high-speed motors have been studied by numerical simulations and experiments. Nevertheless, the cooling systems of the motor often requires auxiliary equipment such as fans, heat exchangers, and oil pumps, which reduces the reliability and cost-effectiveness of the motor.

To summarize, the heat transfer characteristics of the cooling medium under specific air gap structure, axial Reynolds number, or Taylor number, many scholars have been thoroughly investigated by numerical simulation, experiments, and theoretical analysis. Nevertheless, the axial Reynolds number and Taylor number of compressed natural gas in the air gap of high-speed induction motor are 9.02×10^3-2.41×10^4 and 3.53×10^9-1.7×10^{11}, respectively. The ratio of the inner radius to the outer radius of the air gap of the natural gas-cooled high-speed induction motor is 0.971. Therefore, the

results of the existing studies cannot be used to describe the flow of natural gas in the air gap of high-speed induction motors. It is necessary to further investigate the flow and heat transfer characteristics of compressed natural gas in the air gap of natural gas-cooled high-speed induction motors. In this study, based on the numerical heat transfer theory, a stator-air gap-rotor geometric model of the motor is established by the finite volume method. The multi-condition coupling mechanism of the motor and the cooling medium are taken into consideration, and the evolution of the high-pressure natural gas flow pattern in the air gap is explored. Then, the variation law of flow field and temperature field of the cooling medium in the air gap under different flow patterns is revealed. Additionally, a prediction model of the air gap heat transfer coefficient is established, which provides a theoretical basis for the design of cooling systems of high-speed motors.

2. Numerical model

2.1 Physical model and numerical method

Fig. 1 shows a schematic of the natural gas-cooled high-speed induction motor and its gap. The high-speed induction motor uses a solid rotor. The stator, rotor, and the air gap form an axial cooling air gap, and the heat generation inside the stator and rotor of the motor is mainly carried away by the high-pressure natural gas cooling medium in the air gap, the stator, rotor, and the air gap are numerically calculated. In this study, the following parameters are considered for the air gap model of high-speed asynchronous motor: rated power = 160 kW, rated voltage = 10 kV, and rated speed = 6000 rpm. The outer diameter R_1 of the rotor = 170 mm, the inner diameter R_2 of the stator = 175 mm, the outer diameter R_3 of the stator = 310 mm, the air gap length L = 250 mm, the air gap width $\delta = R_2 - R_1$ = 5 mm, the ratio of inner and outer radius $\eta = R_1/R_2 = 0.971$, the ratio of air gap length to air gap width $\Gamma = L/\delta = 50$, and the radial position $R^* = (R - R_1)/\delta$. R is the radius of any point in the air gap, and its range is 0-1; the axial position is $Z^* = z/\delta$, where z is the distance from any point in the air gap to the entrance, and its value is the range of 0-50.
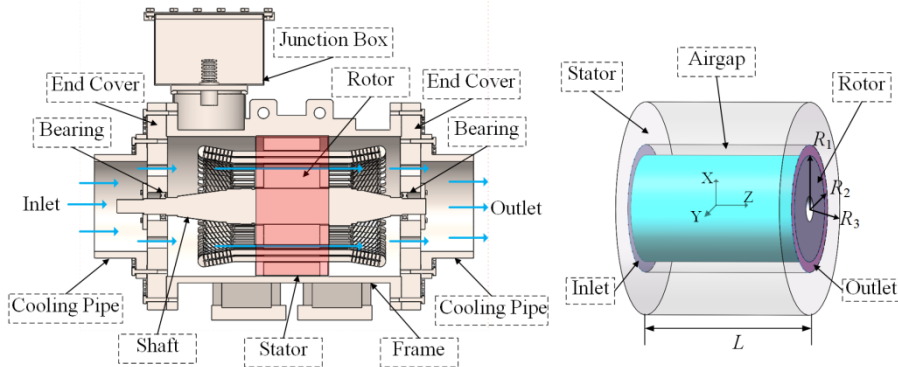

Fig. 1 Schematic of natural gas cooling high-speed induction motor and the physical model of its gap

Numerical simulations were performed using the commercial software Fluent 2020R1. The stator heat source and rotor heat source of the motor were tested, and their electromagnetic losses were 5184 and 5439 W, respectively. The natural gas has a large proportion of methane, in this study, pure methane is used to replace natural gas as the motor cooling medium. The natural gas pressure of the cooling medium was 1, 2, 3, 4, 5, 6, and 7 MPa. The boundary conditions for the mass flow inlets were 0.06, 0.08, 0.1, 0.12, and 0.14 kg/s, and the inlet temperature was 10 °C. The pressure outlet was selected as the outlet; the outer surface of the rotor was set as a rotating wall, and the rotation speed

was set to 6000 rpm to obtain the boundary conditions of 35 working conditions. The coupled algorithm was used for the pressure-speed coupling equation, and the second-order upwind scheme was used for the discretization of the convection term. In the calculation process, the residual error of the flow field was 1×10^{-6}, and the residual error of the temperature field was 1×10^{-8}.

The flow in the air gap of the motor is turbulent. The steady-state control relations for flow and heat transfer are used, including mass, momentum, and energy conservation equations. The shear-stress transport (SST) κ-ω model established by Menter is used as the turbulence model, which can accurately obtain the flow intensity and turbulent kinetic energy in the flow field, and thus the Taylor vortex and turbulent Taylor vortex transition process of the fluid can be obtained [16]. The pressure-velocity coupling equations are solved by coupled algorithm, the discrete format of convection terms use the second-order upwind scheme, the residual of the flow field is 1×10^{-6} and the residual of the temperature field is 1×10^{-8}.

2.2 Mesh independence test

ICEM CFD 2020R1 software was used to divide the geometric model into all hexahedral meshes. The boundary regions of the inner wall of the stator and outer wall of the rotor with large velocity and temperature gradients were encrypted to ensure that y+ < 1. Fig. 2 shows the validation results of mesh independence, where four sets of mesh systems (Mesh1, Mesh2, Mesh3, and Mesh4) are drawn from sparse to dense, and the numbers of meshes are 4.06 million, 5.24 million, 6.67 million, and 8.20 million, respectively. For the case of Reynolds number (Re) = 9890 and Taylor number (Ta) = 4.8×10^{10}, numerical calculations have been performed using the above-mentioned mesh system. When the mesh system is encrypted from Mesh3 to Mesh4, the change in the average heat flux density on the rotor surface with respect to the reference value of Mesh4 is 2.8%. Overall, the grid system Mesh3 is fine enough, and its numerical results are independent in terms of the number of grids. Thus, the Mesh3 grid system is selected for subsequent research. Fig. 3 shows the fluid domain and local grid diagram of Mesh3.
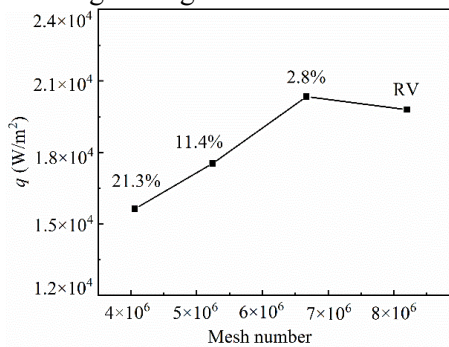

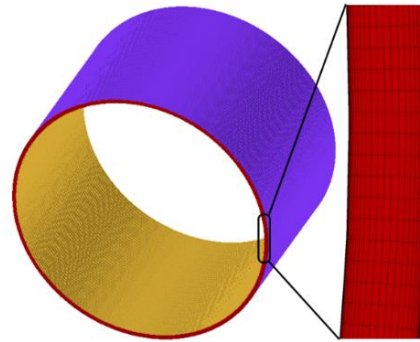**Fig. 2 Results of mesh independence test**   **Fig. 3 Fluid domain and local grid diagram of Mesh3**

2.4. Validation of the numerical method

To verify the accuracy of the proposed numerical method, the calculation results of the Nusselt number (Nu) for the rotor surface under five different Ta are compared with the results obtained using the Tachibana empirical formula [17] in Fig. 4. The maximum deviation between the numerical calculation and empirical results is 7.5%, which indicates that the numerical method used in this paper is reliable and has sufficient precision.
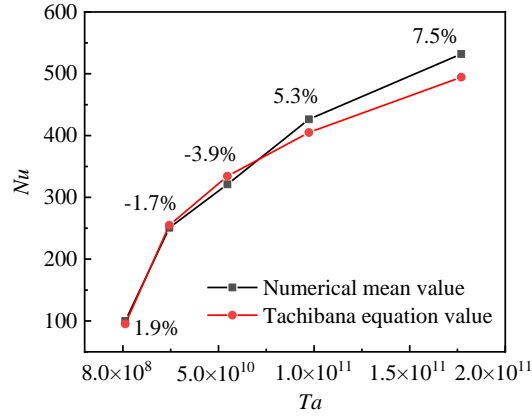
Fig. 4 Verification of *Nu* of the rotor surface

3. Results and discussion

3.1 Flow evolution of natural gas cooling medium in the annular gap

Table 1 shows the orthogonal numerical simulation results of the inlet pressure and mass flow rate in the motor air gap. When the rated speed of the motor is 6000 rpm and the inlet temperature is at a constant value of 10 °C, the air gap inlet pressure of the motor adopts 7 levels, and the mass flow rate adopts 5 levels, which corresponds to 35 motor sites. The 35 motor sites are sorted by Ta/Re^2 values, where the smallest number 1 corresponds to Site 5 and the largest number 35 corresponds to Site 31.

Table 1 The orthogonal numerical simulation results

Sites	Inlet pressure （MPa）	Mass flow rate （kg/s）	Re	Ta	Ta/Re^2	Ta/Re^2 ordering
1	1	0.06	10332	3.53E+09	33	6
2	1	0.08	13776	3.53E+09	19	4
3	1	0.1	17221	3.53E+09	12	3
4	1	0.12	20665	3.53E+09	8	2
5	1	0.14	24109	3.53E+09	6	1
6	2	0.06	10169	1.43E+10	138	14
7	2	0.08	13559	1.43E+10	78	10
8	2	0.1	16949	1.43E+10	50	8
9	2	0.12	20338	1.43E+10	35	7
10	2	0.14	23728	1.43E+10	25	5
11	3	0.06	9984	3.23E+10	325	21
12	3	0.08	13312	3.23E+10	183	17
13	3	0.1	16640	3.23E+10	117	13
14	3	0.12	19968	3.23E+10	81	11
15	3	0.14	23296	3.23E+10	60	9
16	4	0.06	9775	5.76E+10	602	29
17	4	0.08	13033	5.76E+10	339	22
18	4	0.1	16292	5.76E+10	217	18
19	4	0.12	19550	5.76E+10	151	15
20	4	0.14	22808	5.76E+10	111	12
21	5	0.06	9544	8.95E+10	983	32
22	5	0.08	12726	8.95E+10	553	28
23	5	0.1	15907	8.95E+10	354	23
24	5	0.12	19088	8.95E+10	246	19

25	5	0.14	22270	8.95E+10	180	16
26	6	0.06	9292	1.27E+11	1476	34
27	6	0.08	12389	1.27E+11	830	31
28	6	0.1	15486	1.27E+11	531	27
29	6	0.12	18584	1.27E+11	369	24
30	6	0.14	21681	1.27E+11	271	20
31	7	0.06	9022	1.70E+11	2095	35
32	7	0.08	12029	1.70E+11	1178	33
33	7	0.1	15036	1.70E+11	754	30
34	7	0.12	18043	1.70E+11	524	26
35	7	0.14	21050	1.70E+11	385	25

To examine the relationship between the flow state of the natural gas cooling medium and the Ta/Re^2 value in the annular air gap, the vorticity value, number of vortex cells, and the morphological characteristics of the natural gas cooling medium in the air gap are sorted by the 35 working conditions and combined with the velocity isolines. The distribution of vorticity at the meridional plane of the air gap for 35 sites and the distribution of velocity isolines for the typical operating conditions are shown in Fig. 5 and Fig. 6. The 35 sites correspond to three different flow patterns, including the turbulent, spiral Taylor-Couette, and turbulent Taylor-Couette flow. Among them, Sites 5, 4, and 3 correspond to turbulent flow, where the natural gas vorticity in the air gap is basically 0, and the Taylor vortex cell pair is not found. The velocity isoline clouds are a smooth torus. Sites 2, 10, 1, 9, 8, 15, 7, 14, 20, 13, and 6 correspond to spiral Taylor-Couette flow. With the increase in vorticity, irregular Taylor vortex cell pairs appear in the air gap, and their velocity isoline clouds have a spiral toroidal surface. Site 19 and the remaining operating sites correspond to turbulent Taylor-Couette flow. Regular vortex cell pairs appear in the air gap, and the velocity isoline clouds have an annular toroidal surface. With the increase of Ta/Re^2 value, the Taylor vortices appear at the outlet of the air gap (see Site 2), and the number of vortex cell pairs increases and then decreases, while the vorticity increases gradually.
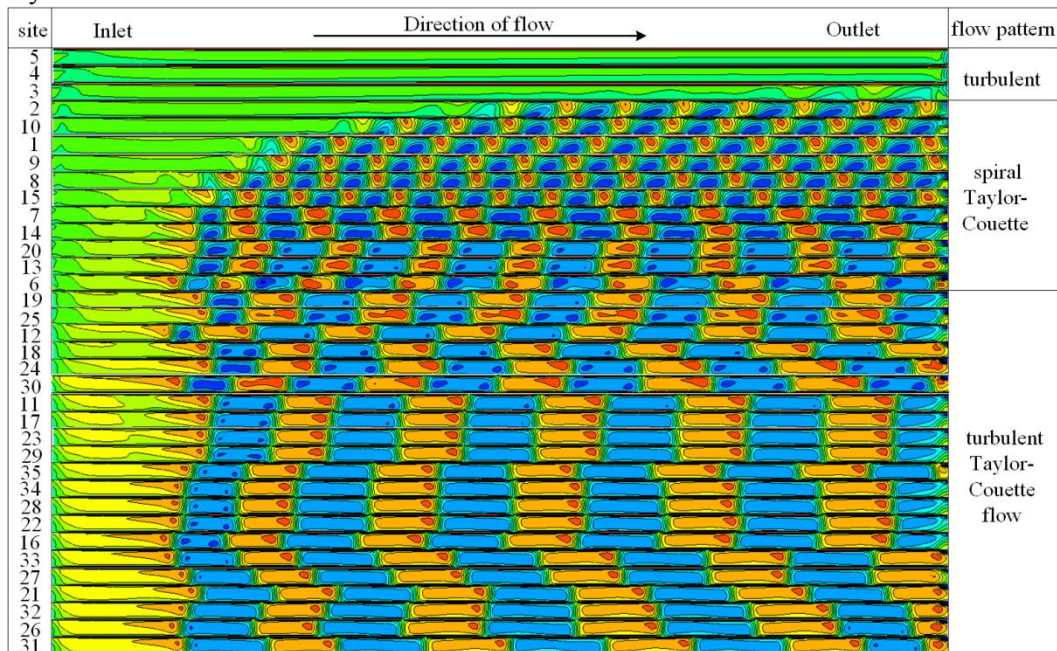

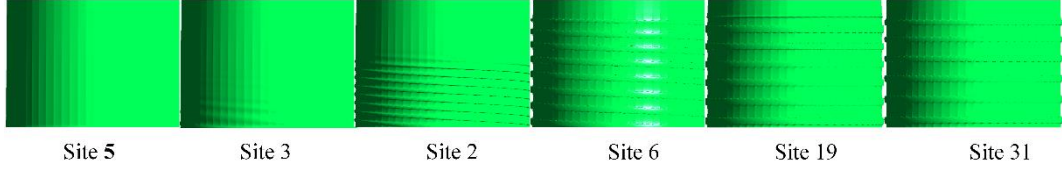**Fig. 5 Distribution of vorticity at the meridional plane of the air gap for 35 sites**

| Site **5** | Site 3 | Site 2 | Site 6 | Site 19 | Site 31 |

Fig. 6 Velocity isolines under typical working conditions

As shown in Table 1 and Fig. 5, the ordering of both Ta/Re^2 ratio and flow pattern for the 35 sites is identical, which indicates that the flow evolution of natural gas in the gap can be reflected by Ta/Re^2 ratio. Therefore, the flow pattern judgment criterion based on Re and Ta is proposed: $\Lambda = Ta/Re^2$, and the Re-Ta flow pattern partition diagram is shown in Fig. 7. The 35 sites are divided into turbulent zone I, spiral Taylor-Couette flow zone II, and turbulent Taylor-Couette flow zone III. When $\Lambda \leqslant 12$, the flow pattern of natural gas in the gap is turbulent (zone I); when $12 < \Lambda < 150$, the flow pattern of natural gas in gap is spiral Taylor-Couette flow (zone II); when $\Lambda > 150$, the flow pattern of natural gas in gap is turbulent Taylor-Couette flow (zone III).
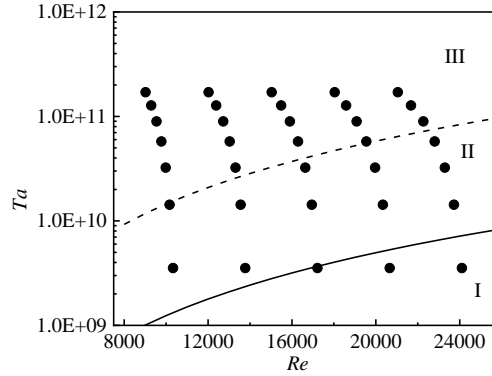

Fig. 7 Re- Ta flow pattern partition diagram

3.2 Influence of flow evolution on the velocity field

To examine the effect of flow evolution of natural gas cooling medium in the annular air gap on the velocity structure, the typical Sites 3, 13, and 33 corresponding to the turbulent, spiral Taylor-Couette, and turbulent Taylor-Couette flow, respectively, are selected. The vortex clouds of the three flow patterns and their local vortex cell pairs are shown in Fig. 8. When the natural gas in the air gap is in the turbulent flow, the vorticity changes dramatically near the inner wall of the stator and the outer wall of the rotor. The vorticity is minimum at the outer wall of the rotor and maximum at the inner wall of the stator, and it gradually increases from the inner wall of the stator to the outer wall of the rotor. In addition to the area near the wall, the vorticity of natural gas in the gap is basically 0, indicating that there is no Taylor-Couette flow in the air gap under turbulent flow. When the natural gas in the gap is spiral Taylor-Couette flow, a spiral Taylor vortex is formed. The vortex cell is rectangular, and the entire air gap is filled in the radial direction. The size of the vortex pair is asymmetric along the axial direction, indicating that the natural gas in the gap is flowing in the axial direction at a helical angle. When the natural gas in the gap is turbulent Taylor-Couette flow, a turbulent Taylor vortex is formed. The vortex cell is rectangular, and the entire air gap is filled in the radial direction. The vortex cell shape is basically symmetrical, indicating that the natural gas in the gap can maintain stable flow in the circumferential direction.
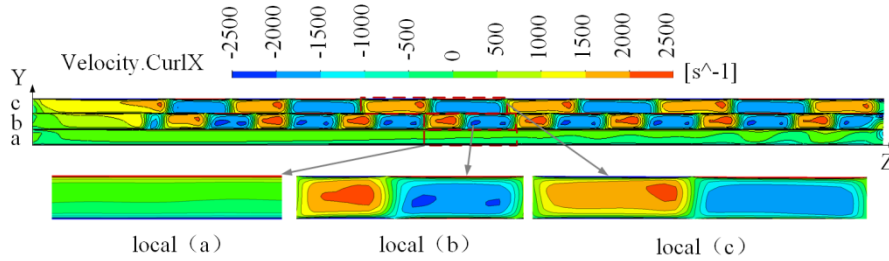
Fig. 8 Vorticity cloud diagram under the three flow patterns and vorticity distribution of the local vortex cell pairs

Fig. 9 shows the velocity streamlines and velocity component isolines of the vortex cell pairs under the local spiral Taylor-Couette flow. The maximum velocity of the spiral Taylor-Couette flow streamlines and circumferential velocity isolines reaches 106 m/s, and the radial and axial velocities are in the range of −4 to 3 m/s, which indicates that the centrifugal force exerted on the natural gas in the gap is dominant. It can be seen that the velocity of the natural gas cooling medium in the vortex cell pairs of the gap is not uniformly distributed along the axial and radial directions, with the maximum velocity near the wall of rotor and minimum velocity near the wall of stator. The radial velocity forms a vortex pair along the axial direction, and the center of the vortex cell is located in the center of the gap. The axial velocity forms vortex pairs along the axial and radial directions, with the axial vortex cell of different sizes and the radial vortex cell of uniform sizes. There is an uneven characteristic of the air gap, which leads to a significant change in the circumferential velocity of natural gas in the gap in the axial direction, showing an irregular convex shape.

Fig. 10 shows the velocity streamlines and velocity component isolines of the vortex cell pairs for local turbulent Taylor-Couette flow. The maximum velocity of the streamlines and circumferential velocity isolines for the spiral Taylor-Couette flow reaches 106 m/s, and the radial and axial velocities are in the range of −4 to 4 m/s. It can be seen that the vortex cell pairs of the gap are symmetrically distributed along the axial direction; the vortex cell velocity is maximum near the wall of rotor and the center of the vortex cell. The radial velocity forms vortex pairs along the axial direction, and the center of the vortex cell is located at the center of the gap. The axial velocity forms vortex pairs along the axial and radial directions, and the vortex cells are the same size. The circumferential velocity shows a regular convex distribution due to the effect of radial and axial velocities on the axial and radial distributions of the gap.
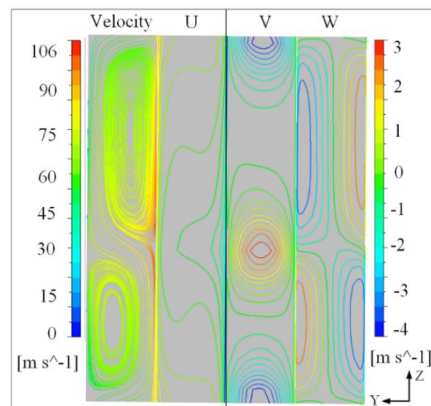

Fig. 9 Velocity streamline diagram for the vortex cell pairs under spiral Taylor-Couette flow and the corresponding velocity component isolines
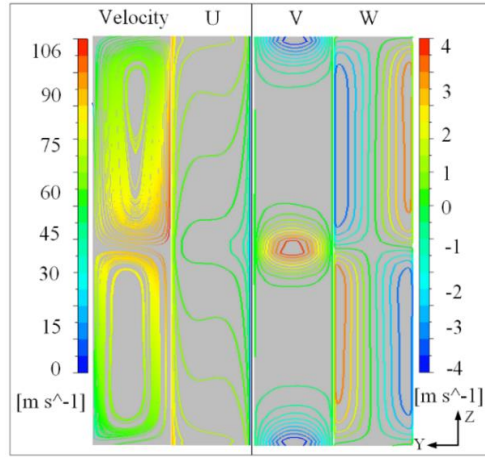
Fig. 10 Velocity streamline diagram of turbulent Taylor-Couette flow vortex cell pairs and the corresponding velocity component isolines

3.3 Effect of flow evolution on the temperature field

To examine the effect of the flow evolution of natural gas cooling medium in the annular gap on the temperature field. The temperature distribution in the meridional plane of the air gap and the temperature distribution of the local vortex cell pairs in the turbulent, spiral Taylor-Couette flow, and turbulent Taylor-Couette flow are shown in Fig. 11. It can be seen that the temperature of the cooling medium in the gap increases along the axial z direction, which is because the high-pressure natural gas cooling medium continuously takes away the heat of the stator and rotor during the flow in the gap. The temperature distributions in the meridional plane for the three flow patterns in the gap are different. Among them, the temperature distribution of the cooling medium in turbulent flow is elliptical, while that in the spiral Taylor-Couette flow and turbulent Taylor-Couette flow is irregularly rectangular.
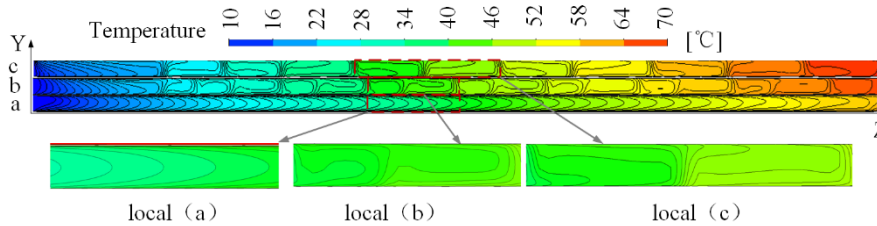

Fig. 11 Temperature profiles in the meridional plane of the air gap for the three flow patterns and their locally magnified views

Fig. 12 shows the temperature distribution on the outer surface of the rotor and the local vortex cell pairs for the turbulent, spiral Taylor-Couette, and turbulent Taylor-Couette flow. It is evident that the temperature distribution under turbulent and turbulent Taylor-Couette flow is circular in the circumferential direction, while that under spiral Taylor-Couette flow is spiral in the circumferential direction, which is consistent with the velocity isoline distributions of the three flow patterns in Fig. 6.
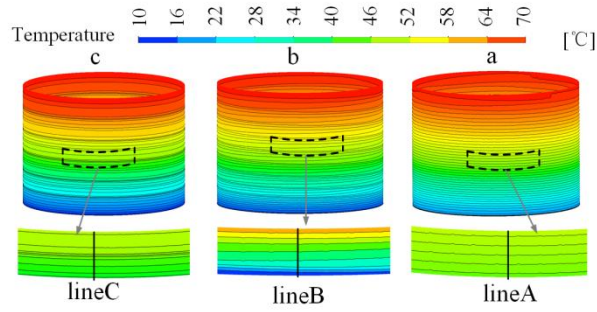
Fig. 12 Temperature distribution on the outer surface of the rotor for the three flow patterns

To further investigate the temperature distribution along the axial direction of the outer surface of the rotor under the three flow patterns, the local lineA, lineB, and lineC temperatures are selected and compared in a dimensionless manner. As shown in Fig. 13, lineA, lineB, and lineC are the dimensionless temperature profiles of the rotor surface for the turbulent, spiral Taylor-Couette, and turbulent Taylor-Couette flow, respectively. It can be seen that when the high-pressure natural gas in the gap is in turbulent flow, the temperature distribution on the rotor surface is linear. When Taylor vortex is formed in the gas gap, the temperature distribution on the rotor surface changes from linear to nonlinear, showing a rapid increase in the center of the Taylor vortex cell pairs. The temperature gradient under the turbulent Taylor-Couette flow is larger than that under the spiral Taylor-Couette flow.
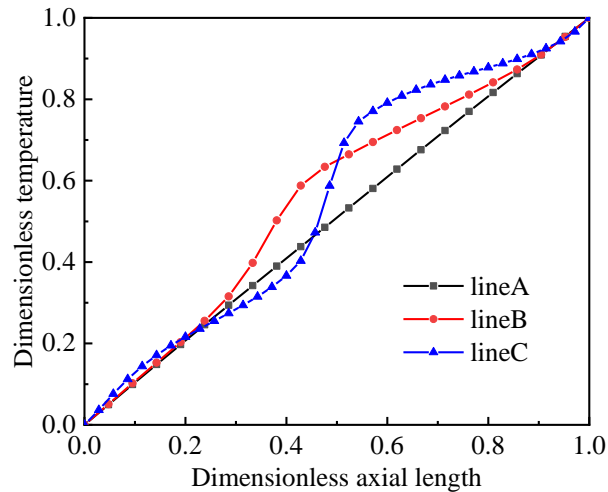

Fig. 13 Surface temperature distribution under the three flow patterns

Fig. 14 shows the heat flux density distributions on the rotor surface and the local vortex cell pairs for the turbulent, spiral Taylor-Couette, and turbulent Taylor-Couette flow. It can be seen that the heat flux density distribution along the circumferential direction is circular under turbulent and turbulent Taylor-Couette flow, while it is spiral under spiral Taylor-Couette flow.
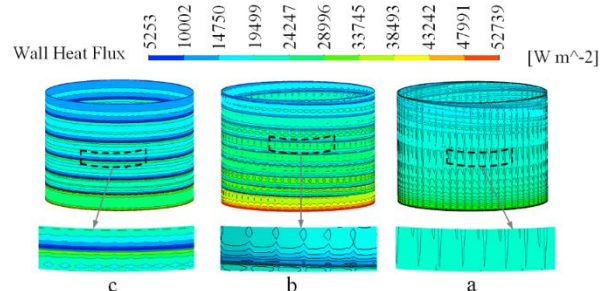

Fig. 14 Distribution of heat flux density on the rotor surface for the three flow patterns

3.4 Prediction model of heat transfer coefficient

Through the numerical simulation results at the 35 sites of the motor air gap. The Nusselt number on the surface of the stator and rotor corresponding to different Reynolds numbers, Taylor numbers, and Prandtl numbers have been calculated. Based on the Levenberg-Marquardt method and global optimization method, the correlation coefficients between the Nusselt number of the motor gap and the mathematical expressions of the Reynolds number, Taylor and Prandtl numbers are obtained: $Nu = ARe^{\alpha}Ta^{\beta}Pr^{\gamma}$, thus the prediction model of the heat transfer coefficient of the motor gap is established.

When the cooling medium in the gap is in a turbulent state, the Nusselt number correlation for the stator surface is

$$Nu = 0.0319Re^{0.3083}Ta^{0.1169}Pr^{-11.7430} \tag{6}$$

In this case, the Nusselt number correlation for the rotor surface is

$$Nu = 1.3316Re^{0.5631}Ta^{-0.1541}Pr^{-11.9621} \tag{7}$$

When the cooling medium in the gap is in a Taylor–Couette flow state, the Nusselt number correlation for the stator surface is

$$Nu = 0.0003Re^{1.0121}Ta^{0.1853}Pr^{0.3036} \tag{8}$$

In this case, the Nusselt number correlation for the rotor surface is

$$Nu = 0.0047Re^{0.9816}Ta^{0.1042}Pr^{1.2545} \tag{9}$$

4. Conclusions

A stator-gap-rotor geometrical model was established to explore the flow and heat transfer characteristics in the air gap of high-speed motors with high-pressure natural gas cooling medium under different working conditions by considering the coupled relationship between the stator heat source, rotor heat source, thermal properties of the cooling medium, and geometrical features of the air gap structure. The main results of the study are summarized as follows:

1) According to the vorticity value of the natural gas cooling medium in the air gap, the number of vortex cells, and their morphological characteristics, combined with the velocity contour map, the three flow patterns in the air gap were determined: turbulent, spiral Taylor-Couette, and turbulent Taylor-Couette flow. And a flow pattern partition method based on Ta/Re^2 was proposed.

2) The influence of the evolution of the three flow patterns on the velocity and temperature fields was revealed. The velocity, temperature, and heat flux density under the spiral Taylor-Couette flow were spirally distributed along the circumferential direction, while the velocity, temperature and heat flux density under the turbulent Taylor-Couette flow were circumferentially distributed. The temperature distributions at the center of the vortex cells for both the spiral Taylor-Couette and turbulent Taylor-Couette flow were nonlinear.

3) By analyzing the numerical results for 35 different working conditions, the relationships between the average Nusselt number and the Reynolds number, Taylor number, and Prandtl number on the inner surface of the stator and the outer surface of the rotor in the annular gap of the natural gas cooling medium were determined, and a prediction model for the flow and heat transfer characteristics in the gap was established to provide a theoretical basis for the design of high-speed motor cooling systems.

References

[1] Li, S. L., *et al.,* High-Speed Electrical Machines: High-Speed Electric Machines: Challenges and Design Considerations, *IEEE Transactions on Industrial Electronics*, *2* (2016), 1, pp. 2-13

[2] Oguz, A. H., *et al.,* Design and Optimization of an Axially-Slitted High-Speed Solid Rotor Induction Motor, 2015 9th International Conference on Electrical and Electronics Engineering (ELECO), Bursa, Turkey, 2015, pp. 568-573

[3] Gao, Q. X., *et al.,* Copper Loss Analysis and Loss Separation Method in a Dynamic Process of Ultra-High Speed Motor with Slotless Stator, *IET Electric Power Applications*, *17* (2023), 4, pp. 464-473

[4] Li, X. L., *et al.,* Incorporating Harmonic-Analysis-Based Loss Minimization into MPTC for Efficiency Improvement of FCFMPM Motor, *IEEE Transactions on Industrial Electronics*, *70* (2023), 7, pp. 6540-6550.

[5] Saari J. Thermal Analysis of High-Speed Induction Machines. Finland: Helsinki University of Technology, 1998.

[6] Naseem, U., *et al.,* Experimental Investigation of Flow Instabilities in a Wide Gap Turbulent Rotating Taylor-Couette Flow, *Case Studies in Thermal Engineering*, *14* (2019), 100449, pp. 1-12.

[7] Tanaka, R., *et al.,* DNS of Taylor-Couette Flow between Counter-Rotating Cylinders at Small Radius Ratio, *International Journal of Advances in Engineering Sciences and Applied Mathematics, 10* (2018), 6, pp. 159-170.

[8] Sznitko, E. T., *et al.,* Flow Dynamics in the Short Asymmetric Taylor-Couette Cavities at Low Reynolds Numbers, *International Journal of Heat and Fluid Flow, 86* (2020), 12, pp. 1-22.

[9] Kusumastuti, A., *et al.,* Characterisation Study of Taylor-Couette Flow in Fluid Mixture of used Cooking Oil and Water, *Journal of Advance Research in Fluid Mechanics and Thermal Sciences, 80* (2021), 2, pp. 106-114.

[10] Fujii, T., *et al.,* Frequency Analysis of Chaotic Flow in Transition to Turbulence in Taylor-Couette System with Small Aspect Ratio, *Journal of Physics: Conference Series, Volume 801, International Conference on Computing and Applied Informatics 2016 14–15 December 2016, Medan, Indonesia, 80* 1(2016), 2, pp. 106-114.

[11] Swann, P. B., *et al.,* Taylor-Couette-Poiseuille Flow Heat Transfer in a High Taylor Number Test Rig, *Journal of the Global Power and Propulsion Society, 5* (2022), pp. 126-147.

[12] Qin, K., *et al.,* Numerical Investigation on Heat Transfer Characteristics of Taylor Couette Flows Operating with CO_2, *Applied Thermal Engineering, 165* (2020), 25, pp. 287-298.

[13] Zhang, J., *et al.,* Design and Thermal Performance Analysis of a New Water-Cooled Structure for Permanent Magnet Synchronous Motors for Electric Vehicles, *Thermal Science, 27* (2023), 3B, pp. 2423-2432.

[14] Xu, Z. Y., *et al.,* Global Fluid Flow and Heat Transfer Characteristics Analysis of an Open Air-Cooled Drive Motor for Drilling Application, *Case Studies in Thermal Engineering, 37* (2022), 102254.

[15] Dong, H. H., *et al.,* Performance of Air/Spray Cooling System for Large-Capacity and High-Power-Density, *Applied Thermal Engineering, 192* (2021), 116925.

[16] Smirnov, P. E., Menter, F. R., Sensitization of the SST Turbulence Model to Rotation and Curvature by Applying the Spalart-Shur Correction Term, *Journal of Turbomachinery, 131* (2009), 4, pp. 041010

[17] Tachibana, F., *et al.,* Convective Heat Transfer of the Rotational and Axial Flow between Two Concentric Cylinders, *Bulletin of JSME*, *7* (1964), 26, pp. 385-391